



Experimental study on collisional disruption of highly porous icy bodies

Yuri Shimaki^{a,*}, Masahiko Arakawa^b

^a Graduate School of Environmental Studies, Nagoya University, Furo-cho, Chikusa-ku, Nagoya 464-8601, Japan

^b Graduate School of Science, Kobe University, 1-1 Rokkodai-cho, Nada-ku, Kobe 657-8501, Japan

ARTICLE INFO

Article history:

Received 23 August 2011

Revised 30 December 2011

Accepted 27 January 2012

Available online 7 February 2012

Keywords:

Ices

Collisional physics

Impact processes

Planetesimals

Comets

ABSTRACT

Knowing the collisional process among small porous icy bodies in the outer solar system is a key to understanding the formation of EKBOs and the evolution of icy planetesimals. Impact experiments of sintered porous ice spheres with 40%, 50%, 60% and 70% porosity were conducted by using three types of projectiles at the impact velocity from 2.4 to 489 m/s, and we studied the effects of porosity on the collisional processes. Projectile sticking occurred at the impact velocity higher than 44 m/s for 60% porosity targets and higher than 13 m/s for 70% porosity targets. The antipodal velocity of the porous ice target increased with the increase of energy density, Q , and it increased slightly with the increase of porosity, although it was exceptionally high in cases when the projectile penetrated the target. The shattering strength of porous ice targets was found to decrease from 100 to 31 J/kg with the increase of porosity from 40% to 70%. The cumulative fragment mass distribution was found to depend on the energy density and the target porosity, and the slopes of the distribution in the small fragment region were almost flat for more porous targets. We reanalyzed the cumulative fragment mass distribution and first obtained the empirical equation showing the fragment mass distribution of porous ice targets as a function of the energy density and the porosity.

© 2012 Elsevier Inc. All rights reserved.

1. Introduction

There are many icy bodies in the outer solar system, such as comets, icy satellites and Edgeworth–Kuiper belt objects (EKBOs). The latter may be formed by a collisional accretion process of icy planetesimals, which are kilometer-sized icy bodies predicted by theoretical studies (e.g., Wada et al., 2009) that are thought to be similar to a comet nucleus. Many impact disruption experiments of non-porous water ice have been performed at impact velocities less than 1 km/s to study the collisional interaction of icy bodies (e.g., Kato et al., 1995; Arakawa et al., 1995), because the average collisional velocity among EKBOs was estimated to be less than 1 km/s (Davis and Farinella, 1997).

Recent ground-based observations and spacecraft explorations for small solar system bodies have revealed that many asteroids and comets have significantly large porosity. The porosities of explored asteroids are now estimated to be from a few percent up to 65% when the material density of a corresponding meteorite is assumed for each asteroid (e.g., Britt et al., 2002, 2006). Comet nuclei are usually expected to have porosities larger than 30%. For example, the bulk porosity of comet Tempel-1 is estimated to be about 60%. This estimate might be applicable to other comet nuclei,

such as Wild 2 and Borrelly, because highly porous structures could be a common feature for comet nuclei. Therefore, experimental studies on the collisional disruption of small bodies have been conducted recently related to not only asteroids but also small icy bodies to clarify the effect of porosity on the critical impact specific energy.

In the study of collisional disruption, the energy density, Q , defined by the kinetic energy of a projectile divided by a target mass is a typical parameter used to describe the impact condition. The critical impact specific energy for dispersion, Q_D^* , is the energy density required for catastrophic disruption of the body when the self gravity is taken into account. However, the re-accumulation of impact fragments by the self gravity cannot be treated in laboratory experiments. The critical impact specific energy for shattering, Q_S^* , is given by the Q value where the resulting largest fragment mass is one-half of the original target mass, and Q_D^* is suggested to be the sum of Q_S^* and the gravitational energy of the colliding body (e.g., Davis et al., 2002). The results of experiments in laboratory-scale impacts cannot be applied to planetary scale impacts directly, so that numerical simulations are necessary to study them (e.g., rubble pile formation and Q_D^*). Laboratory experiments are necessary to construct scaling laws for impact disruption, and the results of such experiments can help to improve the numerical models.

Love et al. (1993) carried out high-velocity impact experiments on sintered glass beads targets with various porosities up to 60%

* Corresponding author. Fax: +81 78 803 5791.

E-mail address: shimaki@eps.nagoya-u.ac.jp (Y. Shimaki).

and found that the shattering strength increased with increasing porosity and that the strength was proportional to $(1 - \phi)^{-3.6}$, where ϕ denotes the porosity. The shattering strength could be affected by the physical mechanisms depending on porosity, which are related to shock pressure decay and pore crashing. This effect of strengthening the target with the porosity was also found in other porous materials such as gypsum, mortar (Davis and Ryan, 1990), crushed ice aggregates (Ryan et al., 1999; Giblin et al., 2004) and porous pure ice (Arakawa et al., 2002). Arakawa et al. (2002) conducted low-velocity fragmentation experiments on synthetic porous pure ice targets with porosity up to 55%, and they found that the shattering strength of a pure ice target increased with the porosity and was proportional to $(1 - \phi)^{-1.6}$. Moreover, they succeed to explain the porosity dependence of the shattering strength of pure ice according to their theoretical model, which related to physical processes such as shock pressure attenuation and failure stress, based on P_1 scaling law (Mizutani et al., 1990). We discussed detail of this model in Section 4.1.

The degree of sintering, characterized by bonding strength among constitutive grains, has been found to play an important role in the collisional disruption process in addition to the porosity. Setoh et al. (2007) performed low-velocity disruption experiments with a sintered glass beads target that had a fixed porosity of about 40%, while the static strength ranged within two orders of magnitude. They found the empirical relationship between the static compressive strength (Y) and the shattering strength (Q^*) for the sintered glass beads as shown by $Y \propto Q^*$, although the obtained Q^* was one order of magnitude smaller than that obtained for high-velocity experiments (Love et al., 1993). A similar relationship between Y and Q^* was also found in our previous study for a sintered porous ice target with a constant porosity of 40% (Shimaki et al., 2011). We changed the static compressive and tensile strength of sintered snow by almost one order of magnitude, and then the shattering strength was found to be proportional to the static strength.

Recent numerical and laboratory experiments on the planetesimal formation process suggest the possibility of the existence of highly porous icy bodies through the collisional sticking of icy dusts and their aggregates. Suyama et al. (2008) and Wada et al. (2009) performed a series of numerical simulations associated with collisional growth and fragmentation of fractal dust aggregates composed of submicron ice particles, and they concluded that icy dust aggregates could survive through the mutual collisions among small icy bodies at the impact velocity up to 50 m/s without compaction, that is, the formation of km-sized extremely porous icy planetesimals is feasible. The laboratory experiment using micrometer-sized ice dust aggregates showed that the specific surface energy of micrometer-sized ice dust was 0.190 J m^{-2} (Gundlach et al., 2011), and this value was about twice as large as the previously measured value used in Wada et al. (2009), which also supports the possibility of the formation of highly porous icy planetesimals. However, the collisional process of icy planetesimals is still unclear, because there are no impact experiments of ice targets with porosity larger than 55%. Therefore, it is important to conduct laboratory experiments related to the collisional process of highly porous bodies to understand the formation process of icy planetesimals, and the findings may be applicable to the collisional growth process of icy planetesimals to larger icy bodies.

In this paper, we report our impact experiments of sintered porous ice sphere targets with the porosity between 40% and 70%, in which the ice or snow projectiles had an impact velocity from 2.4 to 489 m/s. The effect of porosity on the collisional type, fragment velocity, mass distribution and shattering strength were clarified, and we propose a new empirical equation to describe the cumulative fragment mass distribution for porous bodies.

2. Experimental methods

2.1. Sample preparation

Porous ice targets with different porosities were prepared by using ice particles in a cold room at -15°C . The targets were spheres, 60 mm in diameter, in which the porosity was changed from 40% to 70%. The ice particles used to construct the targets were less than $250 \mu\text{m}$ in diameter. The ice particles were prepared by freezing small water droplets in liquid nitrogen. The droplets were made using a special spray that can produce water droplets with an average diameter of $28 \mu\text{m}$ with a standard deviation of $12 \mu\text{m}$. These ice particles were put into a spherical mold with a diameter of 60 mm. To change the target porosity, we changed the mass of ice particles put into the mold from 62.4 to 32.1 g. Ice particles in the mold were compressed gently at a pressure up to 1 MPa to form a homogeneous spherical target. After the compression, the snow target was taken out of the mold and preserved in a sealed plastic bag at a temperature of -15°C , and the sample was sintered for a period from 1 h to 1 month. The target had a homogeneous interior, without density fluctuation, and a smooth spherical surface. The experimental conditions are summarized in Table 1.

Ice and porous ice projectiles were used in this experiment. A porous ice cylindrical projectile with 30% porosity, a diameter of 10 mm and a mass of 0.35 g and a porous ice spherical projectile with 30% porosity, a diameter of 15 mm and a mass of 1.14 g were each sintered for one day at -15°C . These porous ice projectiles were made of the same type of ice particles used for the target preparation. They were also prepared in a mold and then sintered in a plastic bag. A cylindrical ice projectile with a diameter of 15 mm, a height of 10 mm and a mass of 1.6 g was used at an impact velocity larger than 300 m/s, because the snow projectile was broken during the acceleration above this velocity range.

2.2. Impact experiments

Impact experiments were conducted by using vertical gas guns set in a large cold room of the Institute of Low Temperature Science, Hokkaido University (Fig. 1). The projectiles were launched at velocities from 30 to 490 m/s, and a head-on collision between the projectile and the target was achieved in all experiments. The room temperature was regulated to be $-15 \pm 0.5^\circ\text{C}$ during the experiments. The gas guns can accelerate a projectile with a diameter of 10 mm up to 186 m/s, and a projectile with a diameter of 15 mm up to 489 m/s. A large sample chamber was evacuated below 0.1 bar at the impact velocity faster than 300 m/s to prevent the projectile from being affected by air drag. A laser-beam system was installed in a chamber to measure the projectile velocity (e.g., Arakawa et al., 1995). In addition to the gas gun, a spring gun was used to accelerate a projectile from 9.7 to 17 m/s, and a free-fall method was used at the impact velocity from 2.4 to 3 m/s.

The target was suspended by threads in a cubic acrylic box with a side of 30 cm to recover impact-produced fragments. To avoid secondary collisions, which occur when impact fragments collide with the box walls, we set sponge plates on three sides and the bottom of the box. However, the front of the box was not covered by a sponge plate, to allow observation by a high-speed digital video camera. When a projectile cut off the laser beam in front of the box, an actuator released the threads and the target was dropped in free fall. After the shot, we recovered the impact fragments and sieved them to sort the fragments. We picked up impact fragments larger than 2 mm and measured their masses by an electric balance. The fragments with the size of 0.7–2 mm were gently sieved, and this sieving process might have damaged porous

Table 1
Experimental conditions and results.

Run number	m_p (g)	M_t (g)	V_t (m/s)	Q (J/kg)	m_i/M_t	V_a (m/s)	V_a/V_g^b	Collisional types	Sintering duration
<i>Porosity = 40%</i>									
10-1217-2	0.30	62.22	2.70	0.018	1.000	–	–	Rebound	1 day
10-1217-3	0.30	62.22	2.81	0.019	1.000	–	–	Rebound	1 day
10-1217-9	0.30	62.22	13.2	0.42	1.000	–	–	Rebound	1 day
10-1217-8	0.34	62.22	16.6	0.75	1.000	–	–	Rebound	2 day
10-1221-1	0.35	61.65	66.3	12	0.930	0.38	1.0	Cratering	5 days
10-1219-2	0.32	62.30	98.6	25	0.850	0.48	0.9	Cratering	2 days
09-1104-4	0.36	62.05	115	39	0.965	0.65	0.97	Cratering	1 h
09-1104-1	0.35	62.38	122	41	0.955	0.53	0.77	Cratering	1 day
09-1104-2	0.35	62.09	152	65	0.785	0.55	0.65	Cratering	1 day
09-1105-1	0.35	61.96	154	67	0.734	0.46	0.53	Cratering	1 h
09-1110-6	0.35	62.04	182	94	0.647	0.76	0.74	Cratering	1 week
09-1104-3	0.35	62.20	184	95	0.915	0.91	0.88	Cratering	1 day
09-1105-2	0.37	62.28	186	103	0.553	0.86	0.78	Cratering	1 h
09-1110-8	1.09	62.12	100	88	0.490	1.8	1.01	Disruption	1 week
09-1106-2	1.18	62.13	115	126	0.273	1.6	0.75	Disruption	1 h
09-1105-5	1.18	62.28	121	139	0.171	1.9	0.85	Disruption	1 day
09-1105-3	1.03	61.86	146	178	0.307	2.2	0.88	Disruption	1 day
09-1110-7	1.09	61.98	155	210	0.203	2.7	0.99	Disruption	1 week
09-1106-1	1.15	62.07	168	260	0.229	1.9	0.63	Disruption	1 h
09-1106-3	1.15	62.16	203	380	0.146	4.0	1.07	Disruption	1 h
09-1110-9	1.09	62.08	214	403	0.352	4.1	1.08	Disruption	1 week
09-1108-3	1.13	61.88	214	419	0.144	3.8	0.98	Disruption	1 day
09-1105-4	1.17	62.04	217	446	0.193	n.d.	–	Disruption/(no video)	1 day
09-1110-10	1.59	61.87	248	790	0.171	7.3	1.14	Disruption	1 week
09-1211-4	1.57	61.71	269	921	0.072	8.7	1.27	Disruption	1 month
09-1108-2	1.59	62.09	291	1086	0.164	n.d.	–	Disruption/(no video)	1 day
09-1106-4	1.62	62.01	301	1183	0.101	10.2	1.30	Disruption	1 h
09-1108-1	1.66	62.06	313	1309	0.095	9.9	1.18	Disruption	1 day
09-1110-11	1.59	61.90	452	2630	0.043	17.2	1.48	Disruption	1 week
09-1110-12	1.59	62.36	467	2775	0.029	17.5	1.47	Disruption	1 h
09-1109-2	1.58	62.05	489	3039	0.054	18.2	1.46	Disruption	1 day
<i>Porosity = 50%</i>									
10-1217-4	0.30	51.82	2.35	0.02	1.000	–	–	Rebound	1 day
10-1218-1	0.34	51.93	16.2	0.86	1.000	–	–	Rebound	2 days
09-0624-6	0.34	51.96	25.8	2.2	0.999	0.1	0.66	Rebound	1 h
10-1221-2	0.34	51.87	58.5	11	0.979	0.42	1.10	Rebound/cratering	5 days
09-0624-4 ^a	0.30	52.00	73.5	16	0.599	0.7	1.65	Cratering	1 h
09-0623-4 ^a	0.30	52.00	86.6	22	0.643	0.7	1.34	Cratering	1 h
09-0623-3 ^a	0.32	51.90	105	34	0.395	0.8	1.30	Disruption	1 h
09-0624-5	0.32	52.00	143	63	0.568	1.1	1.29	Cratering	1 h
09-0624-7	0.33	51.89	160	82	0.230	1.5	1.44	Disruption	1 h
09-1210-1	1.10	51.75	94	92	0.232	2.0	1.00	Disruption	1 day
09-1210-2	1.10	51.81	163	282	0.091	3.9	1.13	Disruption	1 day
09-1210-3	1.10	51.92	201	429	0.090	11.5	2.71	Disruption	1 day
09-1210-4	1.60	51.54	280	1203	0.076	13.9	1.62	Disruption	1 day
09-1210-5	1.60	51.44	452	3150	0.022	25.9	1.86	Disruption	1 day
<i>Porosity = 60%</i>									
10-1217-5	0.30	41.41	2.52	0.023	1.000	–	–	Rebound	1 day
10-1219-4	0.34	41.42	14.5	0.86	1.000	–	–	Rebound	2 days
10-1218-2	0.32	41.42	14.5	0.81	1.000	–	–	Rebound	2 days
10-1219-5	0.31	41.42	28.7	3.1	1.000	0.27	1.27	Rebound	2 days
09-0624-1	0.35	41.00	43.9	8.2	1.003	n.d.	–	Sticking/(no video)	1 day
10-1220-3	0.33	41.19	71.4	20	0.971	0.37	0.65	Cratering	4 days
09-1211-8	0.32	41.32	90.0	31	0.779	0.5	0.75	Cratering	1 month
10-1220-2	0.34	41.42	90.1	33	1.006	0.47	0.64	Sticking	3 days
09-0624-2	0.32	41.64	102	40	0.920	1.0	1.30	Cratering	1 day
09-1110-1	0.39	41.17	125	74	0.638	1.0	0.82	Cratering	1 week
09-1211-6	0.35	41.55	126	67	0.651	0.9	0.84	Cratering	1 month
09-0624-3	0.30	41.05	139	70	0.562	1.4	1.41	Cratering	1 day
09-1110-2	0.32	41.37	147	84	0.434	1.6	1.38	Disruption	1 week
09-0625-7	0.34	41.34	162	107	0.331	1.6	1.17	Disruption	1 day
09-0618-2	1.10	43.39	25.6	8.3	0.997	0.7	1.01	Rebound	1 day
09-0618-3	1.14	43.57	85.2	95	0.204	3.3	1.49	Disruption	1 day
09-1210-7	1.10	40.49	111	166	0.286	13.7	4.58	Penetration	1 month
09-1109-4	1.14	41.18	119	195	0.114	11.6	3.54	Penetration	1 week
09-1210-6	1.10	40.97	150	300	0.087	24.6	6.14	Penetration	1 month
09-1109-1	1.05	40.68	158	322	0.090	19.0	4.65	Penetration	1 week
09-0618-1	1.15	42.97	158	335	0.104	5.7	1.34	Disruption	1 day
09-0618-4	1.16	43.60	182	440	0.096	8.5	1.75	Disruption	1 day
09-1211-1	1.10	41.58	193	497	0.081	40.5	7.84	Penetration	1 month
09-1109-5	1.16	41.26	203	578	0.058	38.1	6.69	Penetration	1 week
09-1211-5	1.59	41.41	137	359	0.109	23.8	4.52	Penetration	1 month

(continued on next page)

Table 1 (continued)

Run number	m_p (g)	M_t (g)	V_i (m/s)	Q (J/kg)	m_i/M_t	V_a (m/s)	V_a/V_g^b	Collisional types	Sintering duration
09-1211-2	1.60	41.67	271	1430	0.024	25.6	2.42	Disruption	1 month
09-0619-1	1.59	41.92	283	1519	0.025	20.4	1.90	Disruption	1 day
09-1109-6	1.55	41.13	297	1662	0.037	31.3	2.80	Disruption	1 week
09-1211-3	1.60	41.53	451	3971	0.012	50.4	2.86	Disruption	1 month
09-1109-3	1.58	41.05	462	4099	0.012	n.d.	–	Disruption/(no video)	1 week
Porosity = 70%									
10-1217-7	0.32	31.05	2.52	0.033	1.000	–	–	Rebound	1 day
10-1217-6	0.30	31.05	3.08	0.030	1.000	–	–	Rebound	1 day
10-1218-6	0.30	31.00	9.66	0.45	1.000	0.094	1.00	Rebound	2 days
10-1218-7	0.30	31.00	10.0	0.48	1.000	0.081	0.84	Rebound	2 days
10-1218-3	0.30	31.09	14.0	0.95	1.010	0.23	1.72	Sticking	2 days
10-1218-4	0.30	31.39	15.0	1.1	1.000	0.16	1.10	Rebound	2 days
10-1218-5	0.30	31.39	15.6	1.2	1.010	0.16	1.06	Sticking	2 days
10-1220-4	0.34	30.90	34.5	6.5	0.996	n.d.	–	Sticking/(no video) ^a	4 days
10-1220-6	0.35	31.13	61.3	21	1.005	0.27	0.40	Sticking	4 days
09-0625-2	0.33	30.99	70.2	26	1.005	n.d.	–	Sticking/(no video)	3 days
10-1220-7	0.34	30.97	71.0	28	0.996	0.58	0.74	Sticking ^a	4 days
09-0625-4	0.32	31.20	71.1	26	1.006	0.6	0.80	Sticking	3 days
10-1220-5	0.34	31.08	76.1	32	0.787	0.7	0.79	Cratering	4 days
09-0625-1	0.31	30.96	91.2	42	0.190	1.2	1.32	Disruption	3 days
09-0625-3	0.33	30.59	96.9	51	0.335	1.3	1.27	Disruption	3 days
09-0623-2	0.31	31.00	103	53	0.359	2.6	2.51	Disruption	3 days
09-0625-6	0.31	31.56	139	95	0.290	1.8	1.32	Disruption	3 days
10-0616-6	1.10	31.17	3.82	0.3	1.000	0.22	1.61	Rebound	2 days
10-0616-7	1.20	31.17	13.4	3.4	1.000	0.44	0.86	Rebound	2 days
10-0616-2	1.19	31.43	77.9	115	0.112	16	5.46	Penetration	2 days
10-0616-1	1.17	31.14	86.0	139	0.090	23	7.06	Penetration	2 days
09-0626-1	1.10	30.95	167	494	0.128	50.0	8.44	Penetration	3 days
09-0627-1	1.02	31.07	190	592	0.046	59.1	9.48	Penetration	3 days
09-0627-2	1.67	31.12	297	2367	0.050	52.9	3.32	Disruption	3 days
10-0616-4	1.60	30.89	469	5691	0.006	77	3.16	Disruption	2 days

^a The data of m_i/M_t on Fig. 9 was excluded because the fragment mass distribution was calculated based on the experimental conditions: The target was divided into two comparable large fragments.

^b V_g is the velocity of center-of-mass and was calculated from experimental condition.

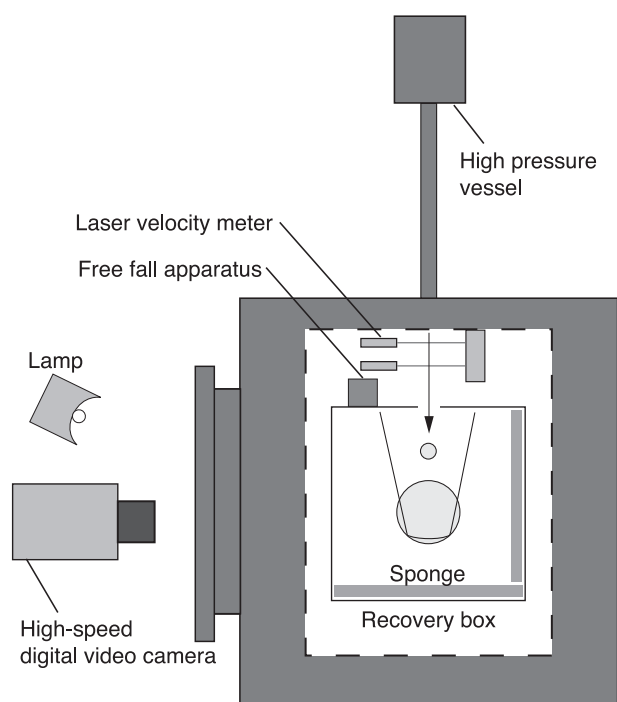


Fig. 1. Schematic illustration of the experimental setup. The target was suspended in a recovery box by strings connecting to a free-fall apparatus, which released the sample when a projectile cut a witness laser. Sponges set on the walls prevented fragments from secondary fragmentation on the walls.

ing process was not large, and thus it did not affect the fragment mass distributions significantly. It was difficult to measure the masses of individual fragments with a diameter smaller than 2 mm, so we measured the total mass of these small fragments. The number of fragments was estimated by dividing the total mass left on the sieve by the mass of one piece of the fragments. The collisional disruption was recorded by high-speed digital video cameras (NAC MEMRECAM-fx RX-6, K3). The shutter speed was 10 or 20 μ s, and the frame rate was from 10^3 to 10^4 frames per second. The image size of the recorded video was 512×384 pixels for 10^3 fps, 640×200 pixels for 5×10^3 fps and 512×248 pixels for 10^4 fps. The typical spatial resolution of the recorded image was 0.5 mm/pixel for 10^4 fps. The video camera observed the target perpendicular to the impact direction. We used two metal halide lamps to illuminate the target, and these lamps were installed beside the camera to gain a sufficient brightness for high-speed photography.

3. Results

3.1. In situ observation of collisional phenomena

The collisional phenomena such as disruption, cratering and sticking were recorded by a high-speed digital video camera, and the recorded images enabled us to analyze the motion of well-separated impact fragments in detail. We measured the velocity distribution of the ejected fragments to classify the collisional outcomes discussed below for each impact experiment. We classified the collisional outcomes as rebound, sticking, cratering, catastrophic disruption, and penetration type collisions. Since the collision type strongly depended on the impact velocity and the target porosity, we show the in situ observation of collisional phenomena for

ice fragments and changed the fragment size; however, even for the 70% porosity sample, the damage to the fragments by the siev-

targets with porosity from 40% to 70% in the low-, middle- and high-velocity regions.

Fig. 2a (top) shows snapshots taken at 10 ms after the impact in the low-impact velocity region, 70 m/s. There are four snapshots corresponding to the collisions for the target porosities of 40%, 50%, 60% and 70%. The spherical porous ice targets were struck by cylindrical porous ice projectiles of 0.35 g with 30% porosity. In this low-velocity region, we never observed catastrophic disruption of the target for any of the porosities. Rebounding, cratering and sticking had occurred in these cases, and the types appeared depending on the porosity. For the 40% and 50% porosity target, the projectile did not disrupt after the impact, and it rebounded with the restitution coefficient of 0.08 for the 40% porosity target and 0.036 for the 50% porosity target, where the restitution coefficient was defined as the ratio of the rebound velocity to the impact velocity of the projectile in the normal direction. The 40% porosity target was cratered at the impact site, and a large crack was initiated from the impact site. The crack grew outward to form a few large fragments with a dish-like shape, which were ejected at several m/s. For the 50% porosity target, the target was divided into two large hemispheres, and a small dish-shaped fragment was ejected from the impact point. For the 60% porosity target, the pro-

jectile almost did not rebound from the target, which meant a restitution coefficient of 0.014, but it did not stick and was not captured by the target. The target was cracked at the impact site as was shown in the 40% porosity target and formed a dish-shaped large fragment. The targets with 40% and 60% porosity were slightly broken around the impact site but mostly remained intact, so we classified this type of collisional outcome as cratering. Based on these observations, we defined cratering as the collisional outcome showing the largest fragment mass larger than a half of the initial target mass. For the 70% porosity target, the projectile penetrated the target and was captured in the target interior. We called this type of collisional outcome sticking. The ejected fragment mass from the impact site was so small that the mass of the recovered target increased about 0.2 g because of the captured projectile.

Fig. 2b (middle) shows snapshots taken at 2 ms after impact at the middle-impact velocity region, 200 m/s, and the porous ice sphere projectile with a mass of 1.1 g was used for each shot. All targets were catastrophically disrupted so that a large number of fine fragments were formed during the impact. It is very noticeable that the shape of the envelope made of the expanding fragments is very different between 40/50% porosity targets and 60/70% porosity targets. For 40% and 50% porosity targets, we can observe severe fractures around the impact site. For these targets, a large number of small fragments were ejected from the cratered region, while the region far from the impact site was not so fractured and several large fragments were generated and ejected slowly. We call this type of collisional outcome catastrophic disruption. For 60% and 70% porosity targets, we hardly observe any ejecting fragments from the impact site. Instead, we can observe a bullet-like envelope accelerating with high velocity toward the downstream from the antipodal point. Thus, small and fine fragments were generated around the antipodal point, while most of the target was moderately disrupted to generate large fragments. It is impressive that radial cracks aligning with equidistance appeared on the 60% porosity target. These characteristics could have been caused by the projectile penetration of the target, because we can see a small block that resembles a projectile at the head of the ejecta envelope. It is obvious that the expanding velocity of the envelope from the antipode for the 70% porosity target is higher than that for the 60% porosity target. This may have been caused by the difference in the deceleration force being proportional to the target density against the projectile for each porosity target. We call this type of collisional outcome penetration.

Fig. 2c (bottom) shows snapshots taken at 0.8 ms after the impact in the high-impact velocity region, 450 m/s, and ice cylindrical projectiles with a mass of 1.6 g were used for the shot. For the 40% and 50% porosity targets, the features of the ejecta envelope were very similar to those of middle-impact velocity region qualitatively. The difference of the ejecta envelope in Fig. 2c from that in Fig. 2b is clearly recognized in the targets with 60% and 70% porosity, that is, we never observe apparent penetration by the projectile. This change might have been caused by the projectile fragmentation during the impact, because the intact ice projectile was never recovered after the shot. The fragmented projectile could have been captured in the target, because the penetration depth was shallower than the target length. In the next section, we briefly summarize collisional outcomes.

3.2. Collisional types

Direct sticking among porous bodies is an important mechanism of pre-planetary growth in the solar nebula. In this study, we found that this process occurred under the limited impact condition. To determine this physical condition, the collisional types featured during and after the impact were divided into five types.

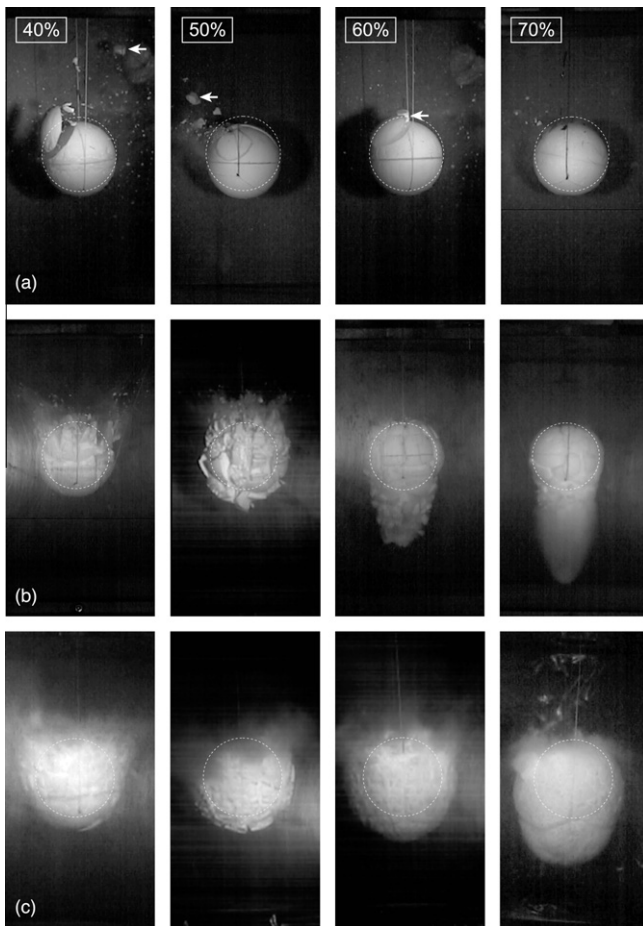


Fig. 2. Snapshots of collisional phenomena for the targets with porosity from 40% to 70%. They were impacted at the same impact velocity (V_i) in each figure, but the target porosity varied. The time after impact is (a) 10 ms, (b) 2 ms and (c) 0.8 ms, respectively. Dotted white circles show the initial position of the target. (a) $V_i = 70$ m/s. The run number of each shot is 101221-1 for $\phi = 40\%$, 090623-4 for $\phi = 50\%$, 101220-3 for $\phi = 60\%$ and 090625-4 for $\phi = 70\%$. A white arrow shows the position of a rebounded projectile. (b) $V_i = 200$ m/s. The run number of each shot is 091110-9 for 40%, 091210-3 for 50%, 091109-5 for 60% and 090627-1 for 70%. (c) $V_i = 450$ m/s. The run number of each shot is 091110-11 for 40%, 091210-5 for 50%, 091211-3 for 60% and 100616-4 for 70%.

Fig. 3 briefly summarizes experimental results in the form of a collisional type diagram shown by the impact velocity and the target porosity for a similar projectile mass: the projectile mass was (a) 0.35 g, (b) 1.1 g and 1.6 g. Each type is classified by the two parameters showing the degree of disruption and the penetration effect: the largest fragment mass normalized by the original target mass (m_l/M_t) and the antipodal fragment velocity normalized by the velocity of the center of mass (V_a/V_g). They are rebound at $m_l/M_t = 1$, sticking at $m_l/M_t > 1$, cratering at $1 < m_l/M_t < 0.5$, catastrophic disruption at $m_l/M_t < 0.5$ and penetration at $m_l/M_t < 0.5$ with $V_a/V_g > 3.5$. Details about the fragment mass and velocity are discussed in the next sections.

In Fig. 3a, for the smallest projectile with the mass ratio of the projectile to target, $m_p/M_t = 0.0056$ – 0.011 , the sticking was found at the impact condition for the target porosity larger than 60%; it occurred at the impact velocity between 44 and 90 m/s for the target with 60% porosity and at the impact velocity between 13 and 71 m/s for the target with 70% porosity. However, this sticking condition disappeared at the larger mass ratio of $m_p/M_t = 0.018$ – 0.051 , as shown in Fig. 3b, when the disruption and penetration appeared at the same velocity and porosity range. The reason for this apparent difference in the sticking region depending on the m_p/M_t is not clear, but we speculate that a critical penetration depth might be necessary for sticking in this porosity range. We found that typi-

cally, the penetration depth corresponding to the projectile diameter was necessary for sticking. Therefore, when the penetration depth was sufficiently deep for sticking, the larger projectile caused a larger energy density to disrupt the target, and thus the sticking type does not appear in Fig. 3b.

Instead of sticking, penetration was observed in Fig. 3b at the impact velocity between 78 and 203 m/s for targets with 60% and 70% porosity. Boundary A between the penetration and the disruption for these targets could have been caused by the projectile disruption, and thus this boundary was determined to be 203–271 m/s, as shown by the dotted line.

Cratering was observed between boundaries B and C in Fig. 3a. Boundary B corresponds to the upper limit velocity of the rebound in each porosity target, the velocity if which was 29 m/s for the 60% porosity target. Taking into account the porosity dependence of the tensile strength, in which strength increases with decreasing porosity (e.g., Mellor, 1975), the boundary velocity could increase with decreasing target porosity, as shown by the dashed line.

Boundary C, corresponding to the impact condition for the catastrophic disruption, Q^* , is shown by a bold line in Fig. 3a and b. This boundary will be discussed in the following sections in detail.

In the following sections, we examine the fragment velocity and mass distributions for the collisional types of cratering, catastrophic disruption and penetration.

3.3. Fragment velocity distribution

Fig. 4 shows snapshots of the impact disruption at 2.4 ms after the impact for targets with 40% and 70% porosity. We measured the velocity vectors of fragments in a two-dimensional coordinate system by tracing the motion of well-identified fragments. A black circle shows the original position of the target. We determined the initial position angle θ of surface fragments by measuring these velocity vectors. The angle was set to be zero degrees at the antipode of the impact point and was scaled between $\pm 180^\circ$. White arrows show the velocity vectors of identified fragments, and the cross points of these arrows with the initial target circle were determined to be the initial positions of these fragments on the target surface. The arrow length corresponds to the fragment velocity,

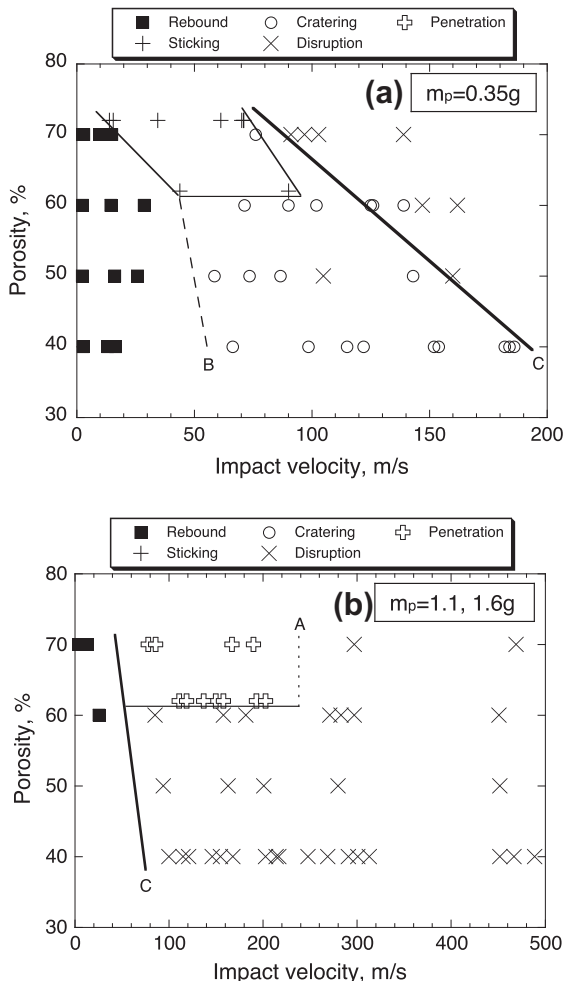


Fig. 3. Collisional outcomes shown in the relationship between the impact velocity and the target porosity: they are rebound, cratering, penetration, sticking and catastrophic disruption after the impact. (a) The impact diagram for the projectile of 0.35 g, and (b) the impact diagram for the projectile of 1.1 g and 1.6 g.

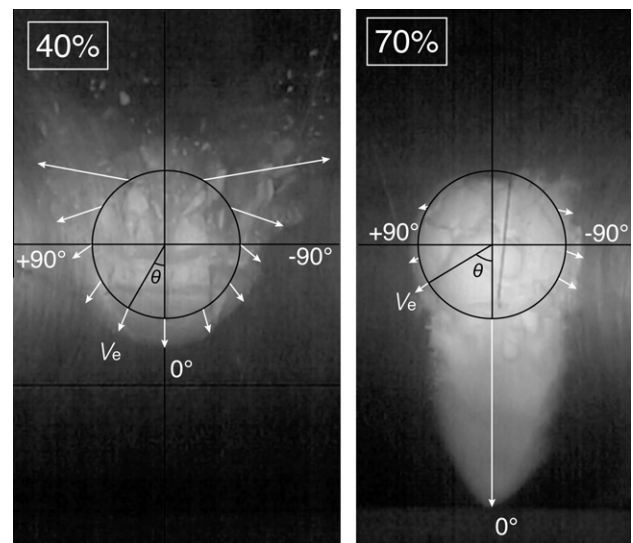


Fig. 4. 2-D velocity vectors of impact fragments originally located on the target surface with 40% porosity (091106-3) and 70% porosity (090626-1). Both images are snapshots taken 2.4 ms after the impact. Targets were impacted at 167 m/s for the 40% porosity target and at 206 m/s for 70% porosity target. A black circle denotes the initial position of the target, and the angle of the fragment original position θ on the target surface is measured from the antipodal point, $\theta = 0^\circ$.

V_e , and all of the vectors around the antipodal point are extrapolated and merged to be almost one point for the 40% porosity target; this point is called the irradiation point, and it is an imaginary point of ejection origin of these fragments (Paolicchi et al., 1989). In the 70% porosity targets, the position of the irradiation point determined from the fragments originating near the impact site is fairly different from that determined from the fragments near the antipodal point: the irradiation point moves from near the impact point to the center of the target, depending on the initial fragment position angle θ .

Fig. 5a shows fragment velocity distributions of the target with 40% porosity impacted at different energy densities from 39 to 2275 J/kg. For energy densities from 39 to 103 J/kg, the collisional type was rebound or cratering, so most of the target mass moved at the same velocity as the antipodal velocity. Thus only one velocity was plotted at 0° for these non-destructive targets. At energy densities higher than 210 J/kg, the fragment velocity distribution shows a flat pattern at $\pm 90^\circ$, which means that fragment velocities were almost constant on the hemisphere, including the antipodal point. In this situation the ejecta envelope looks like an expanding balloon. But, near the impact site at the angle of $\pm 150^\circ$, the fragment velocity suddenly increases, owing to the effect of the crater formation process.

Fig. 5b shows the fragment velocity distribution for targets with 70% porosity. At the energy density from 3 J/kg to 32 J/kg, the collisional mode was sticking or cratering, so the target was almost intact and was measured to move at the velocity of the center of the mass system, V_g . At energy densities higher than 115 J/kg, the fragment velocity at 0° corresponding to the antipodal velocity

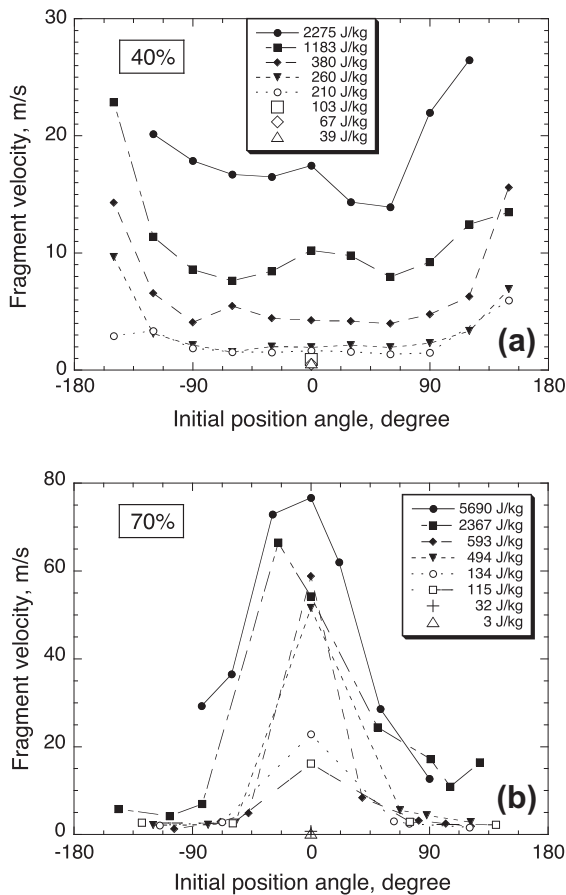


Fig. 5. Velocity distributions of the impact fragments for targets with porosity of: (a) 40% and (b) 70% as a function of θ . The fragment velocity at the θ of $\pm 180^\circ$, which is the position near the impact point, could not be obtained.

was clearly higher than V_g and exhibited the maximum in each velocity distribution (see Table 1). The maximum velocity increased with the increase of energy density. This feature that the antipodal velocity showed the maximum fragment velocity is the opposite of what is normally observed for non-porous brittle materials, which is that the antipodal velocity of basalt and ice is the slowest velocity in the fragment velocity distribution (Fujiwara and Tsukamoto, 1980; Arakawa, 1999). This velocity distribution with a peak at the antipodal point is also found in the 60% porosity targets shown in Fig. 2b. Therefore, the antipodal velocity with the maximum fragment velocity and the relatively low fragment velocity around the impact crater are the most obvious features of the impact disruption of highly porous ice targets.

3.4. Antipodal velocity

Fig. 6 shows the relationship between the antipodal velocity and the energy density. The open symbols indicate the target porosities for the penetration type collisions, and the closed or crossed symbols mean the target porosities of the rebound, sticking, cratering and catastrophic disruption type collisions, which we call the non-penetration group. In several experiments for the 60% porosity target impacted at the same Q value, we observed both the penetration and the non-penetration type collisions (see Fig. 3b), which might have been caused by a small difference in the compressive strength of the projectile. Each data set with different target porosity was fitted by a power law equation to examine the effect of target porosity and the collisional type on the antipodal velocity. The following empirical equation was obtained by fitting each data set:

$$V_a = \alpha Q^\beta, \quad (1)$$

where V_a is the antipodal velocity in the unit of ms^{-1} , Q is the energy density in the unit of J/kg and α and β are constants. The fitted parameters α and β are summarized in Table 2. In the data sets of the penetration group with 60% and 70% target porosity, the antipodal velocity is about one order of magnitude higher than that of the non-penetration group (Fig. 6). Furthermore, it is clearly observed that the antipodal velocity of the 70% porosity targets is slightly higher than that of the 60% porosity targets systematically. In the data sets of the non-penetration group, the antipodal velocity is almost identical to that of the center of the mass system at the energy density below a few 100 J/kg, irrespective of the target porosity, and the empirical equations of the porosity targets are very close to each other and also close to that of non-porous water

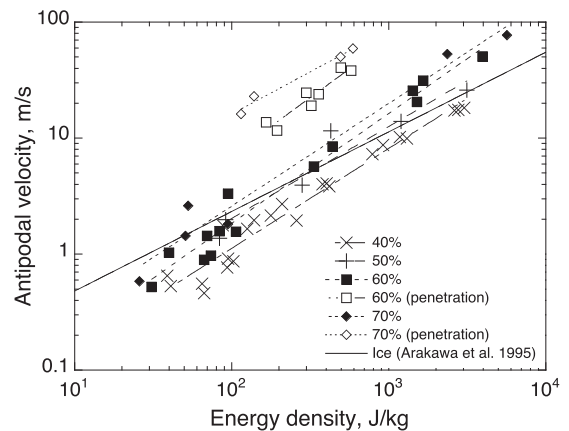


Fig. 6. Relationship between the energy density and the antipodal velocity for porous ice targets compared with non-porous ice (Arakawa et al., 1995). Open symbols indicate the collisional type of penetration for 60% and 70% porosity.

Table 2

The results of fitting the coefficient for Eq. (1).

Porosity (%)	Group	α (J/kg) $^{-\beta}$	β
40	Non-penetration	$10^{-1.54 \pm 0.09}$	0.81 ± 0.04
50	Non-penetration	$10^{-1.19 \pm 0.08}$	0.79 ± 0.08
60	Non-penetration	$10^{-1.32 \pm 0.13}$	0.82 ± 0.06
70	Non-penetration	$10^{-0.84 \pm 0.10}$	0.63 ± 0.06
60	Penetration	$10^{-1.13 \pm 0.37}$	0.99 ± 0.15
70	Penetration	$10^{-0.25 \pm 0.18}$	0.73 ± 0.07

ice: they are scattered within a factor of 3. However, our analysis clarified that the antipodal velocity weakly depends on the target porosity, and it increases with the increase in the target porosity.

3.5. Fragment mass distribution

After each impact experiment, we recovered all the impact fragments dispersed from the target in the recovery box. Fig. 7a shows the mass distributions of the recovered fragments from the targets with 40% porosity, which were impacted at velocities from 115 to 467 m/s, corresponding to energy densities from 39 to 2775 J/kg. These fragment distributions are shown in the form of the relationship between the cumulative fragment mass normalized by the original target mass (m_c/M_t) and the fragment mass normalized by the original target mass (m/M_t). The cumulative fragment mass is defined as the total mass of the fragments that is smaller than the fragment mass. The maximum value in the horizontal axis of each distribution represents the normalized largest fragment mass, and the minimum value in the horizontal axis represents the total mass of the fine fragments that is smaller than about 0.01% of the

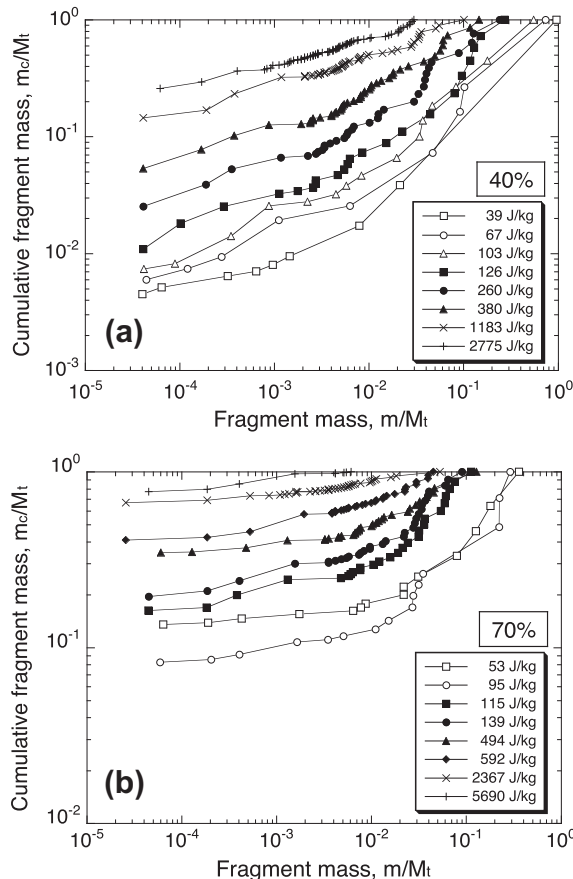


Fig. 7. Cumulative fragment mass distribution for targets with porosity of: (a) 40% and (b) 70%.

original target mass. The systematic change of the mass distribution is clearly observed in both the largest fragment and the fine fragments. The largest fragment of each distribution decreases with the increase of the energy density, and the total amount of the fine fragments increases with the increase of the energy density. We noticed that each mass distribution of the 40% target was similar to that of non-porous water ice with the same largest fragment mass (Arakawa, 1999).

Fig. 7b shows the fragment mass distributions of the targets with 70% porosity. We found that the slope of the distribution of 70% porosity targets was flatter than that of 40% porosity targets. This means that middle-size fragments could be easily broken during the impact and separated into individual ice particles that were originally used to prepare our porous ice targets. The similar mass distribution was already observed in the previous study of snow impact experiments for 55% porosity targets by Arakawa et al. (2002). Furthermore, the total amount of fine fragments of 70% porosity targets is larger than that of 40% porosity targets at a similar energy density. These features indicate that the snow targets with 70% porosity are more fragile and that their impact fragments could be separated into original ice particles easier than those of 40% porosity targets.

It is interesting to examine the effects of the sintering duration on the mass distribution of the impact fragments, because our previous study clarified that the mass distribution systematically changed with the sintering duration for 40% porosity snow targets composed of crushed ice grains smaller than 700 μm (Shimaki et al., 2011). In an investigation of this effect, snow targets with 40% porosity were impacted at a constant energy density of about 300 J/kg after 1 h or 1 week of sintering at -15°C (Fig. 8). In Fig. 8, the present results are compared with the results obtained from targets made of 700- μm ice particles sintered for 1 month at -15°C (Shimaki et al., 2011). We found that these three distributions showed good agreement with each other at m_i/M_t larger than 0.01, irrespective of the ice particle size and the sintering duration, indicating that 90% of the fragments had the same distribution. This shows that the fragment mass distribution is independent of the sintering duration in our experiments, but it is inconsistent with our previous results, which strongly depended on the sintering duration (Shimaki et al., 2011). This difference could be explained by the grain size dependence on the neck growth rate among ice grains (Maeno and Ebinuma, 1983). In our small ice grains with the size of several 10 μm , these necks quickly grew to nearly maximum size within the experiment's time scale, which was less than 1 h in the current experiment but more than 1 month

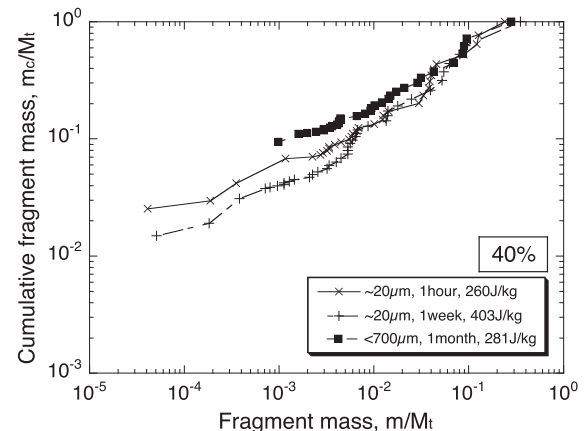


Fig. 8. Cumulative fragment mass distributions for targets with a constant porosity of 40%, which were constructed of ice particles with different sizes and sintered for different durations. The mass distribution for a 700- μm ice particle target was from Shimaki et al. (2011).

for the 700- μm ice grain targets, so the 1-week distribution is almost the same as the 1-h distribution. Therefore, in this study our sintered target with the same porosity composed of small ice grains could have the similar shattering strength irrespective of the sintering duration.

3.6. Largest fragment mass and impact strength

The normalized largest fragment mass is the most typical parameter to describe the degree of impact fragmentation. Fig. 9 shows the relationship between the normalized largest fragment mass and the energy density for the target with porosity from 40% to 70%. Non-porous ice data obtained by Arakawa et al. (1995) and basalt data compiled by Takagi et al. (1984) are also plotted for reference. Note that all of the data sets for the porous ice target are below the basalt line and are mixed with crystalline ice data set, because the slopes of the relationship for the crystalline ice and basalt are steeper than that of porous ice targets. As with the results of the mass distributions, the largest fragment mass decreases with the increase of the energy density and also decreases with the increase of the target porosity. As a result, each data set regardless of porosity is well merged and can be fitted by a power law equation as follows:

$$\frac{m_1}{M_t} = q_0 \cdot Q^p. \quad (2)$$

The fitted values of the coefficients q_0 and p for each data set are summarized in Table 3. The p of the snow targets is systematically smaller than that of crystalline ice. The data in Fig. 9 looks somewhat scattered, but the power-law fitting on these data is able to justify the dependence on the porosity. The shattering strength,

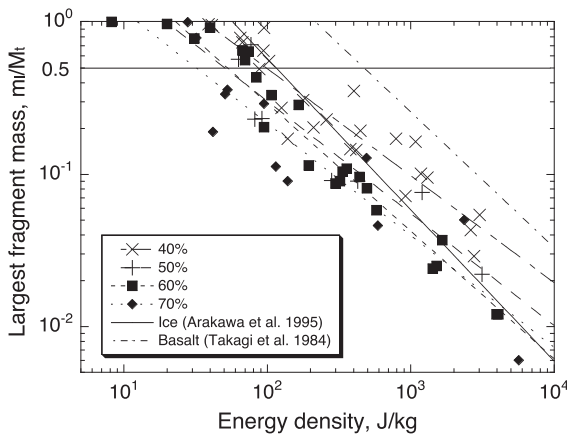


Fig. 9. Relationship between the normalized largest fragment mass and the energy density. The non-porous ice result taken from Arakawa et al. (1995) is shown as a solid line, and the basalt result taken from Takagi et al. (1984) is shown as a dashed-dot line.

Table 3
The results of fitting the coefficient for Eq. (1).

Porosity/target	q_0 (J/kg) $^{-p}$	p	Q^* (J/kg)
40%	$10^{1.10 \pm 0.14}$	-0.70 ± 0.06	100 ± 7
50%	$10^{0.92 \pm 0.29}$	-0.74 ± 0.12	51 ± 14
60%	$10^{1.14 \pm 0.11}$	-0.84 ± 0.04	52 ± 6
70%	$10^{0.79 \pm 0.24}$	-0.73 ± 0.10	31 ± 9
Ice	$10^{1.7}$	-1.0	110
Basalt	$10^{2.1}$	-0.9	442

Note. The ice data comes from Arakawa et al. (1995), and the basalt data comes from Takagi et al. (1984).

Q^* of each porosity target, where m_1/M_t equals 0.5, is also summarized in Table 3, and it was found to decrease with increasing the porosity. We first quantitatively clarified the porosity dependence of the shattering strength for the snow target with the porosity from 40% to 70%.

Fig. 10 shows the relationship between the filling ratio ($1 - \phi$) and the shattering strength of porous ice targets. The data of the porous ice targets with porosity from 10% to 55% were obtained by recalculating the data of Arakawa et al. (2002), and the data with a constant porosity of 40% sintered for various durations and resulting in different compressive strengths were obtained by Shimaki et al. (2011). It is obvious that the Q^* obtained by the present study decreased with decreasing the filling ratio, and the data can be fitted by a power law equation as follows:

$$Q^* = 10^{2.3 \pm 0.1} (1 - \phi)^{1.5 \pm 0.2}. \quad (3)$$

This empirical equation shows a positive relationship between Q^* and the filling ratio for $\phi > 0.4$, while a negative relationship between them with the exponent of -1.8 for $\phi < 0.55$ was shown by Arakawa and Tomizuka (2004). Thus, we are now able to discuss a wide range of porosity effects on the shattering strength between 0% and 70%. The shattering strength of water ice has a very interesting feature: it reaches maximum at a porosity of around 40% or 55% and then decreases gradually with the increase of the porosity. Section 4.1 includes a detailed discussion of this feature.

In addition to the porosity, the compressive strength, Y_c , of the material has an important role in the collisional disruption process. Fig. 11 shows the relationship between Q^* and Y_c for the porous ice targets with various porosities. The compressive strength used in the present study was estimated from the results of natural snow compiled by Mellor (1975), and the error bars in the compressive strength came from the variety of their data. We found that the Q^* for the porosity larger than 40% obtained by the present study increased with increasing the Y_c and that the data could be fitted by a power law equation as follows:

$$Q^* = 10^{1.9 \pm 0.1} Y_c^{0.27 \pm 0.03}. \quad (4)$$

This relationship could be related to the porosity dependence of Q^* , because the compressive strength strongly depended on the porosity; for the porosity larger than 40%, the Y_c depends on the porosity as $Y_c \propto (1 - \phi)^{5.4}$ (Mellor, 1975). If we substitute Y_c as $(1 - \phi)^{5.4}$ in Eq. (4) we obtain $Q^* \propto (1 - \phi)^{1.5}$, which shows good agreement with

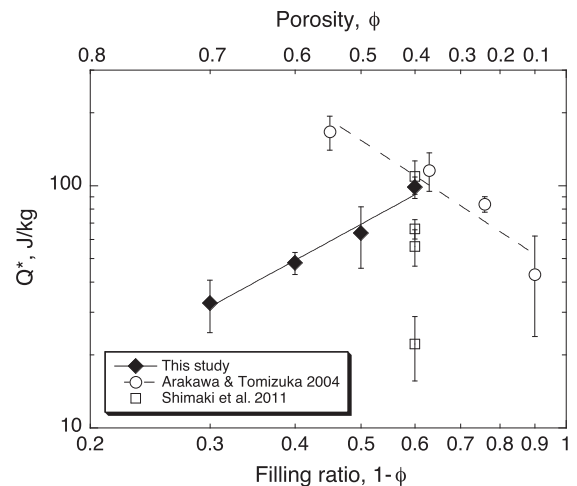


Fig. 10. The shattering strength of sintered porous ice as a function of filling factor, $1 - \phi$. The data for the porosity from 10% to 55% (Arakawa and Tomizuka 2004) and for 40% with four different durations of sintering (Shimaki et al., 2011) are plotted for comparison.

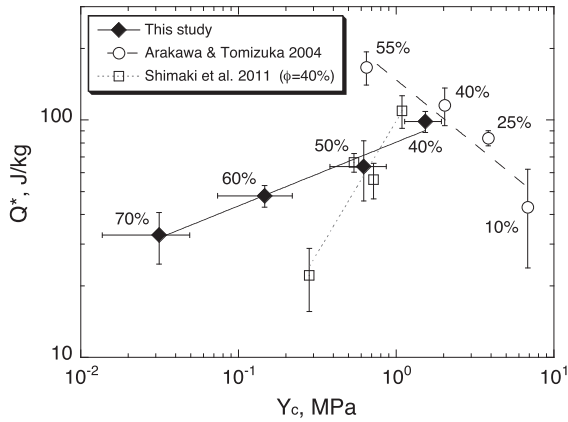


Fig. 11. The shattering strength of sintered porous ice as a function of the compressive strength. The strength data is the same as that listed in Fig. 10. The porosity of each sample is shown in the figure. The compressive strength of each porosity target for present study is estimated from the result of natural snow (Mellor, 1975).

Eq. (3). As described above, the relationship between Q^* and Y_c for porous ice with a constant porosity of 40% sintered for different durations was found to be $Q^* \propto Y_c^{1.1}$ (Shimaki et al., 2011). On the other hand, for porosity smaller than 55% the relationship between Q^* and Y_c was found to be $Q^* \propto Y_c^{0.54}$ (Arakawa and Tomizuka 2004). This behavior could be explained by the weak dependence of Y_c and the strong dependence of the shock pressure attenuation on the porosity, and it is discussed in Section 4.1.

A similar relationship among these parameters was proposed for sintered glass beads by Love et al. (1993) as $Q^* \propto Y_c^{0.45} (1 - \phi)^{-3.6}$. Although there are some differences in the exponents of the compressive strength and the porosity, the large attribution of the porosity on the Q^* is consistent. The differences in the exponents could be caused by the difference in the impact velocity: the impact velocity used in Love et al. (1993) was typically 6 km/s, while in our experiments it was up to 500 m/s. The effect of impact velocity on the shattering strength of porous ice is a subject for future study.

4. Discussion

4.1. Porosity dependence of the impact strength

Fig. 10 shows the interesting relationship between the filling ratio and the shattering strength of porous ice targets. This characteristic behavior of the shattering strength in water ice should be discussed related to physical processes such as shock pressure attenuation and failure stress. A detailed discussion of the porosity dependence of the shattering strength was presented by Arakawa et al. (2002). Eq. (12) in their study showed the effects of porosity on the shattering strength including consideration of the shock pressure decay and the failure stress depending on the porosity, as follows:

$$\frac{Q^*}{Q_{\phi=0}^*} = \left(\frac{P_0}{Y_0}\right)^3 \left(\frac{1}{m_0} - \frac{1}{m}\right) (1 - \phi)^{\frac{3(n-l)-m}{m}}, \quad (5)$$

where m is a shock pressure decay constant that depends on the target porosity, ϕ , described by $m = m_0(1 - \phi)^{-k}$, n is a power law index of the empirical equation for the target dynamic/static compressive/tensile strength, Y , which depends on the target porosity, $Y = Y_0(1 - \phi)^n$, and l is a power law index of the empirical equation for the initial shock pressure, P , which depends on the target porosity described by $P = P_0(1 - \phi)^l$. This means that the initial shock pressure and the material strength decrease with increasing

porosity. Q^* in Eq. (5) is defined as the energy density when non-dimensional scaling parameter P_l , which was proposed by Mizutani et al. (1990), is equal to unity.

Arakawa et al. successfully explained the porosity dependence of the shattering strength in the porosity range from 0% to 40% quantitatively, in which the shattering strength increased with increasing porosity. In their model based on the work of Mizutani et al. (1990), the shock pressure at the antipodal point was compared to the target failure strength to evaluate the shattering strength, and thus the porosity dependencies of the pressure decay constant and the target failure strength are the important parameters needed to reproduce the obtained experimental results. When we use their model to explain our porosity dependence of the shattering strength beyond 40%, we must reconsider the adopted parameter for the target with porosity smaller than 40%. They used $n = 4$, $l = 1.5$, $m = 2(1 - \phi)^{-1/2}$ and $P_0/Y_0 = 100$ for case A, which corresponded to a porous pure ice target. One of the possible ways to successfully reproduce our result is to assume that the parameter m does not change beyond a porosity of 40% and that it remains constant at $\phi = 40\%$. The calculated curve using Eq. (5) is shown in Fig. 12 as a bold line, where we adopted the rule that parameter m was independent of the porosity at ϕ larger than 40%. This figure nicely reproduces our results in Fig. 10, especially the result that the curve has a sharp maximum around 40% porosity. We tried to reproduce our experimental results by changing n , l and m to find possible combinations of these parameters, and found that the most appropriate parameter to reproduce our experimental result of Q^* was that m was a constant of 2.58 for $\phi > 0.4$ with $n = 4$ and $l = 1.5$. The reason why m remains constant for $\phi > 40\%$ is very difficult problem. We think that the attenuation rate of the shock pressure m increases with increasing the porosity, and simultaneously that the penetration depth of the projectile into the target increases because of the weak compressive strength. Thus, we speculated that these two mechanisms competed to determine the m value and the deeper penetration of projectile finally canceled the porosity dependence of m for $\phi > 40\%$. Additionally, we notice in Fig. 12 that the effect of sintering for 40% porosity target should be taken into account in Eq. (5) as a function of sintering duration t in the future.

The existence of a maximum shattering strength at a porosity of about 40% might have an important consequence on the accretion history of icy bodies. At the first stage of the accretion history, icy

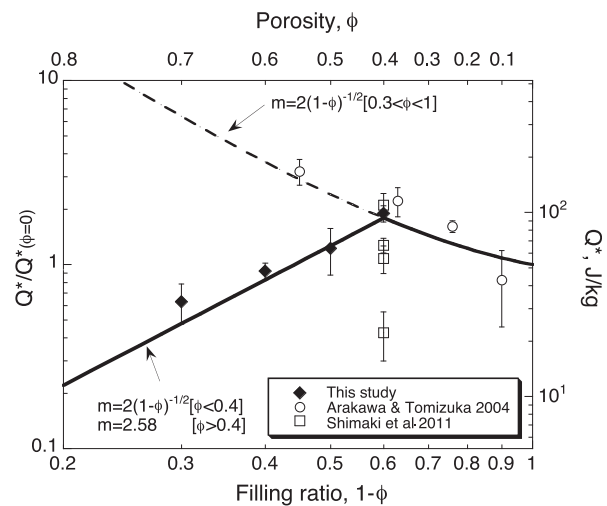


Fig. 12. Normalized impact strength of porous ice targets calculated by Eq. (5). $m = 2(1 - \phi)^{-1/2}$ was used for $\phi < 0.4$ and $m = 2.58$ was used for $\phi > 0.4$ for bold line. Other parameters used in the calculation are $P_0/Y_0 = 100$, $n = 4$ and $l = 1.5$.

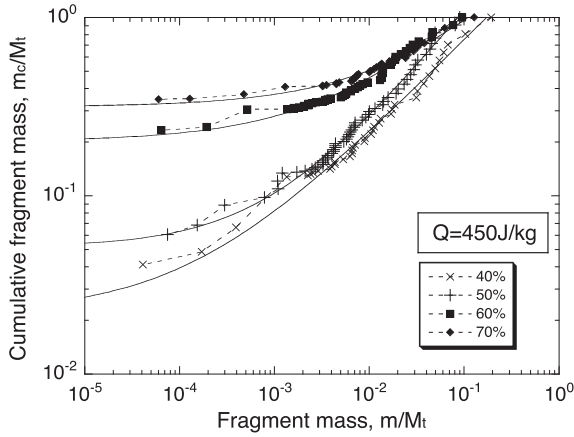


Fig. 13. Cumulative fragment mass distribution for the target with porosity from 40% to 70%. They were impacted at the constant energy density of 450 J/kg. Each distribution is fitted by Eq. (6).

planetesimals could be highly porous bodies, and thus they would be easily shattered and re-accumulated due to the small shattering strength and the small ejection velocities of large fragments with most of the original mass. This indicates the formation of an icy rubble pile body with a large porosity made of both micro and macroporosity. However, as the planetesimals grow and evolve thermally through their accretion history, their porosities would decrease and eventually reach 40% porosity. Thus the shattering of the body would become difficult. Further discussion about the accretion and the thermal evolution of icy planetesimals is needed.

4.2. Modeling of the fragment mass distribution

In this section, we reanalyze the fragment mass distribution and derive the empirical equations related to the impact condition and the target porosity. Fig. 13 shows the cumulative fragment mass distribution for targets with porosity from 40% to 70% and impacted at the same energy density of 450 J/kg. The figure shows clearly that the slope of the distribution in the region where the normalized fragment mass is smaller than 0.01 decreases with increasing porosity, although the largest fragment mass normalized by the original target mass is almost the same for these distributions. To examine this feature quantitatively, the following equation was used to fit these distributions:

$$\frac{m_c}{M_t} = \frac{m_{c-s}}{M_t} + c \left(\frac{m}{M_t} \right)^d, \quad (6)$$

where m_{c-s}/M_t , c and d are the fitting parameters. According to Takagi et al. (1984), they found that the distribution of cumulative fragment number for basalt target was divided into three regions, and in each region the distribution showed a power law relationship depending on the impact condition. Thus, it is reasonable to use a power law relationship to describe the fragment mass distribution in Eq. (6), and in addition to the power law term, we added a constant term independent on the fragment mass because our experimental results showed that the slope of cumulative mass distribution in smaller fragment mass region was almost flat. The fragment mass distribution for each porosity target is fitted by Eq. (6) in Fig. 13, and we find that this equation can approximate each distribution very well. The parameter m_{c-s}/M_t corresponds to the amount of the fragment mass smaller than 0.001% of the original target mass

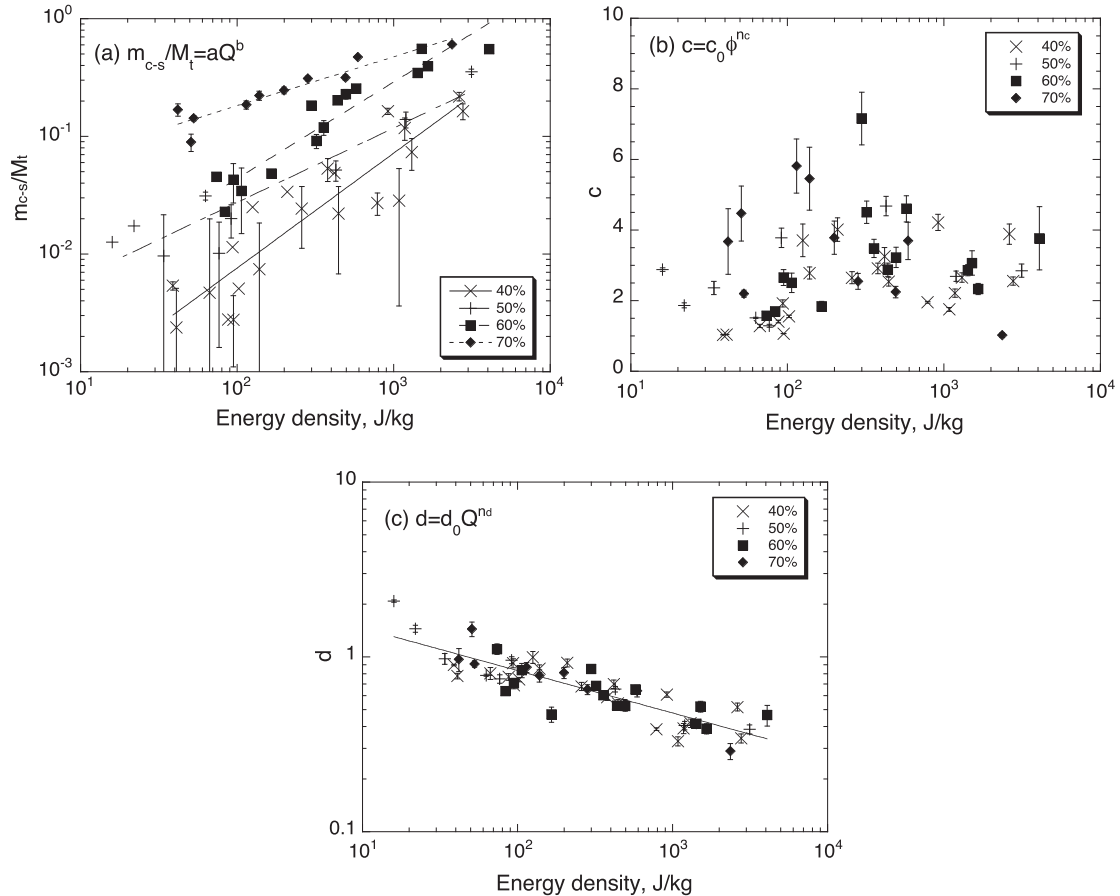


Fig. 14. Relationship between the energy density. (a) m_{c-s}/M_t , (b) c and (c) d in Eq. (6).

corresponding to 0.03–0.06 g, which consists almost entirely of tiny ice grains with the size similar to the initial ice grains.

Fig. 14a shows the relationship between m_{c-s}/M_t in Eq. (6) and the energy density, Q , and it is obvious that m_{c-s}/M_t increases with the increase of Q and the porosity. This trend means that the mass consisting of small fragments corresponding to the initial ice grains increases with the increase of Q and the porosity. In this case, m_{c-s}/M_t can be fitted by a power law equation in each porosity target, and the empirical equation is obtained as follows:

$$\frac{m_{c-s}}{M_t} = a \cdot Q^b. \quad (7)$$

The coefficients a and b for each porosity are shown in Table 4, and the obtained coefficient a strongly depends on the porosity and is found to increase with the increase of porosity from 40% to 70%, that is, about two orders of magnitude, while b slightly decreases with the increase of porosity from 40% to 70%, shown in Fig. 15. Both a and b can be fitted by a power law equation for each porosity, and the empirical equations are obtained as follows:

$$a = a_0 \phi^{n_a}, \quad (8)$$

$$b = b_0(1 - \phi), \quad (9)$$

where the fitted parameters are obtained to be $a_0 = 0.36$, $n_a = 9.0$ and $b_0 = 1.57$.

Fig. 14b shows the relationship between c and Q . We found that c is very scattered between 1 and 8 in the energy density between 10 and 10^4 J/kg and might be independent of Q , but it slightly depends on the porosity and increases with the increase in the porosity from 40% to 70%. Fig. 16 shows the relationship between the porosity and the average value of c , although the error is quite large for each porosity target. The obtained empirical equation is as follows:

$$c = c_0 \phi^{n_c}, \quad (10)$$

Table 4
The results of fitting the coefficient for empirical Eqs. (5) and (6).

Porosity (%)	a	b	c
40	$8.4\text{E-}05$	0.98	2.39 ± 1.01
50	$1.5\text{E-}03$	0.63	2.65 ± 1.08
60	$1.0\text{E-}03$	0.82	3.11 ± 1.43
70	$2.7\text{E-}02$	0.42	4.45 ± 3.52

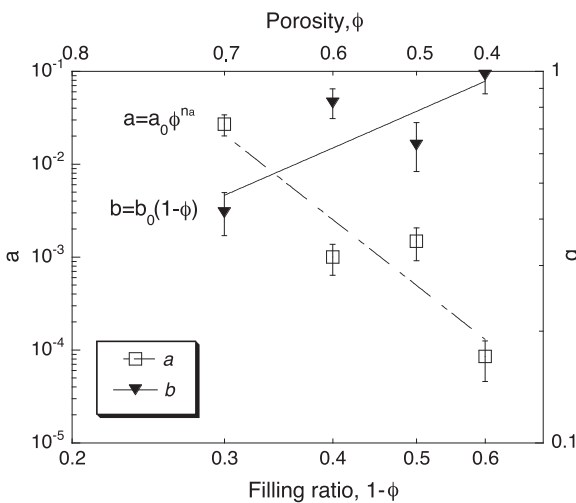


Fig. 15. Porosity dependence of a and power law index b of Eq. (7).

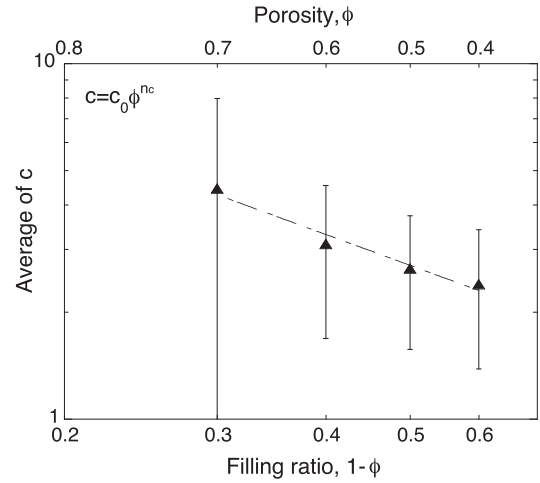


Fig. 16. Porosity dependence of averaged values of c with error bars (1σ).

where c_0 and n_c are fitted to be 5.9 and 1.1, respectively.

Fig. 14c shows the relationship between d and Q , and the figure shows that d is only dependent on the energy density but independent of the porosity and ranges from 0.5 to 1. Here, d is fitted by a power law equation irrespective of the porosities, as follows:

$$d = d_0 \cdot Q^{n_d}, \quad (11)$$

where d_0 and n_d are fitted to be 2.6 and -0.24 , respectively.

According to this analysis, we can propose the fragment mass distribution depending on the energy density, though it is just an empirical relationship in the form of Eq. (6). By combining Eqs. (6)–(11), we obtained the following relationship:

$$\frac{m_c}{m_t} = a_0 \phi^{n_a} Q^{b_0(1-\phi)} + c_0 \phi^{n_c} \left(\frac{m}{M_t} \right)^{d_0 Q^{n_d}}. \quad (12)$$

Each parameter in Eq. (12) is summarized in Table 5. By using Eq. (12) we can reproduce the complete fragment mass distribution for not only the largest fragment mass but also for the middle and small fragment masses. However, we should take care to note the energy density range in which this equation can be applied: it is between 10 and 10^3 J/kg. The experimental results of the fragment mass distribution are compared with Eq. (12) in Fig. 17, and it is obvious that Eq. (12) can reproduce the fragment mass distribution for the targets with 40% and 70% porosity, although Eq. (12) for the 70% porosity target is slightly below the experimental result.

In examining the mass distribution of impact fragments caused by the collision of porous icy bodies, it is important to study not only the re-accumulation process of icy bodies in the solar nebula but also the ice dust generation in the Kuiper belt region and the origin of debris disks around extra-solar nebulae. We have already

Table 5
Summary of equations fitted to the experiments and appropriate parameters.

Physical value	Equation	Parameters
Cumulative fragment mass distribution	(6) $m_c/M_t = m_{c-s}/M_t + c(m/M_t)^d$	c and d
Cumulative mass of finest fragments	(7) $m_{c-s}/M_t = aQ^b$	a and b
Coefficient of Eq. (7)	(8) $a = a_0 \phi^{n_a}$	$a_0 = 0.36$ $n_a = 9.0$
Power of Eq. (7)	(9) $b = b_0(1 - \phi)$	$b_0 = 1.57$
Coefficient of Eq. (6)	(10) $c = c_0 \phi^{n_c}$	$c_0 = 5.9$ $n_c = 1.1$
Power of Eq. (6)	(11) $d = d_0 Q^{n_d}$	$d_0 = 2.6$ $n_d = -0.24$

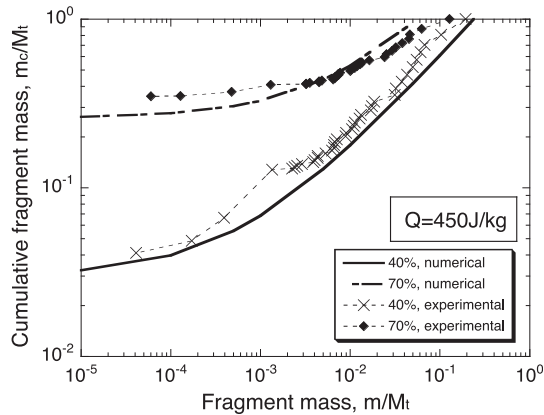


Fig. 17. Fragment mass distributions calculated by Eq. (12) for porous ice targets with 40% and 70% porosity at the constant energy density of 450 J/kg. They are compared with the experimental results and show good agreement with each other.

shown the porosity dependence of the shattering strength (Q^*) on porous ice targets, and a future project will be to study the collisional evolution of these icy bodies by numerical simulations, although it will be challenging to estimate the porosity of icy bodies in the solar nebula and in the Kuiper belt region (Yasui and Arakawa, 2009). Furthermore, an important feature of impact fragments on porous icy bodies, which is that the amount of small fragments (m_{c-s}/M_t) strongly depends on the porosity described by Eq. (6), should be included in the study of ice dust generation by impact. Usually non-porous materials such as ice and rock have a similar fragment mass distribution irrespective of the material type when m_i/M_t is the same, but according to Eq. (6), m_{c-s}/M_t of porous ice targets at the impact strength Q^* of each porosity target changes from 0.007 to 0.10 with increasing porosity from 40% to 70%, where we note that m_i/M_t is defined to be 0.5 at Q^* at each porosity. This drastic change of the small fragment mass due to the porosity would affect the estimation of ice dust generation in solar nebulae, and thus the theoretical study and the numerical simulation of the collisional evolution of icy bodies should be reconsidered while including our results.

Recently, numerical simulations of the collisional disruption and cratering of porous bodies were performed, and the numerical results were compared to the laboratory results for the confirmation of the numerical models (e.g., Juzzi et al., 2008, 2009). These direct comparisons of the laboratory results with the numerical results are desirable to improve the numerical models and to extend the application to various materials, including icy bodies, in future studies.

5. Summary

We carried out impact experiments on sintered porous ice spheres with 40%, 50%, 60% and 70% porosity impacted by three types of projectile at impact velocities from 2.4 to 498 m/s, and we studied the effect of the target porosity and the impact velocity on the collisional types, the velocity and mass distributions of fragments, and the shattering strength. Our results are summarized as follows:

- (1) Projectile sticking occurred at target porosities larger than 60%: we found that the smallest projectile stuck on the target at the impact velocity from 44 to 90 m/s for 60% porosity target and from 13 to 71 m/s for 70% porosity target. However, sticking didn't occur for larger projectiles under the same porosity and velocity conditions; instead, catastrophic disruption or penetration was observed because the energy density was great enough to disrupt the target.

- (2) The antipodal velocity was found to increase with the increase in the energy density and to increase slightly with the target porosity. However, when the projectile penetrated the target, the velocity changed drastically: the antipodal velocity was about one order of magnitude higher than that obtained for the non-penetrated group.
- (3) The shattering strength of porous ice targets was found to decrease from 100 to 31 J/kg with the increase of target porosity. By comparing the results of highly porous ice targets to the results of targets with porosity lower than 40%, we found that the shattering strength of porous ice showed the maximum at the porosity of around 40%. We then tried to explain this feature according to Arakawa et al. (2002), in which the shock pressure attenuation and the failure stress were taken into consideration. We proposed that one possible way to explain our experimental result was that the shock pressure decay constant m increased when the porosity was less than 40% but did not change when the porosity was 40% or greater.
- (4) We obtained the empirical relationship between the shattering strength and the filling ratio for the porosity larger than 40%, as follows:

$$Q^* = 10^{2.3 \pm 0.1} (1 - \phi)^{1.5 \pm 0.2}.$$

- (5) The cumulative fragment mass distribution depended on the energy density and the target porosity. The slope of the distribution at $m/M_t < 0.01$ became gentler with the increase of the porosity and the energy density, and it became almost flat for 70% porosity targets. We reanalyzed the fragment mass distribution by using Eq. (6) and derived the empirical equation of fragment mass distribution described by Eq. (12) as a function of the energy density and the porosity.

Acknowledgments

We thank two anonymous referees for their helpful comments, which guided us in the revision of this manuscript. We are grateful to S. Nakatsubo of the Contribution Division of the Institute of Low Temperature Science, Hokkaido University, for his technical help. This work was supported by a grant-in-aid for scientific research (17340127, 20340118, 22-7305) from the Japan Ministry of Education, Culture, Sports, Science and Technology, and a grant from the Joint Research Program of the Institute of Low Temperature Science, Hokkaido University.

References

- Arakawa, M., 1999. Collisional disruption of ice by high-velocity impact. *Icarus* 142, 34–45.
- Arakawa, M., Tomizuka, D., 2004. Ice-silicate fractionation among icy bodies due to the difference of impact strength between ice and ice-silicate mixture. *Icarus* 170, 193–201.
- Arakawa, M., Maeno, N., Higa, M., Iijima, Y., Kato, M., 1995. Ejection velocity of ice impact fragments. *Icarus* 118, 341–354.
- Arakawa, M., Leliwa-Kopystynski, J., Maeno, N., 2002. Impact experiments on porous icy-silicate cylindrical blocks and the implication for disruption and accumulation of small icy bodies. *Icarus* 158, 516–531.
- Britt, D.T., Yeomans, D., Housen, K., Consolmagno, G., 2002. Asteroid Density, Porosity, and Structure, Asteroid III. University of Arizona Press, Tucson, AZ, pp. 485–500.
- Britt, D.T., Consolmagno, G., Merline, W.J., 2006. Small body density and porosity: New data, new insights. *Lunar Planet. Sci. XXXVII*, 2214 (abstract).
- Davis, D.R., Farinella, P., 1997. Collisional evolution of Edgeworth–Kuiper belt objects. *Icarus* 125, 50–60.
- Davis, D.R., Ryan, E.V., 1990. On collisional disruption: Experimental results and scaling law. *Icarus* 83, 156–182.
- Davis, D.R., Durda, D.D., Marzari, F., Bagatin, A.C., Gil-Hutton, R., 2002. Collisional evolution of small-body populations. In: Bottke, W.F., Jr. et al. (Eds.), *Asteroid III*. University of Arizona Press, Tucson, AZ, pp. 545–558.
- Fujiwara, A., Tsukamoto, A., 1980. Experimental study on the velocity of fragments in collisional breakup. *Icarus* 44, 142–153.

- Giblin, I., Davis, D.R., Ryan, E.V., 2004. On the collisional disruption of porous icy targets simulating Kuiper belt objects. *Icarus* 171, 487–505.
- Gundlach, B., Kilias, S., Beitz, E., Blum, J., 2011. Micrometer-sized ice particles for planetary-science experiments. I. Preparation, critical rolling friction force, and specific surface energy. *Icarus* 214, 717–723.
- Juzzi, M., Benz, W., Michel, P., 2008. Numerical simulations of impacts involving porous bodies. I. Implementing sub-resolution porosity in a 3D SPH hydrocode. *Icarus* 198, 242–255.
- Juzzi, M., Michel, P., Hiraoka, K., Nakamura, A.M., Benz, W., 2009. Numerical simulations of impacts involving porous bodies. II. Comparison with laboratory experiments. *Icarus* 201, 802–813.
- Kato, M., Iijima, Y., Arakawa, M., Okimura, Y., Fujimura, A., Maeno, N., Mizutani, H., 1995. Ice-on-ice impact experiments. *Icarus* 113, 423–441.
- Love, S.G., Hörz, F., Brownlee, D.E., 1993. Target porosity effects in impact cratering and collisional disruption. *Icarus* 105, 216–224.
- Maeno, N., Ebinuma, T., 1983. Pressure sintering of ice and its implication to densification of snow at polar glaciers and ice sheets. *J. Phys. Chem.* 87, 4103–4110.
- Mellor, M., 1975. A Review of Basic Snow Mechanics, vol. 114. IAHA-AISH Pub., pp. 251–291.
- Mizutani, H., Takagi, Y., Kawakami, S., 1990. New scaling laws on impact fragmentation. *Icarus* 87, 307–326.
- Paolicchi, P., Cellino, A., Farinella, P., Zappala, V., 1989. A semiempirical model of catastrophic breakup processes. *Icarus* 77, 187–212.
- Ryan, E.V., Davis, D.R., Giblin, I., 1999. A laboratory impact study of simulated Edgeworth–Kuiper belt objects. *Icarus* 142, 56–62.
- Setoh, M., Nakamura, A.M., Hirata, N., Hiraoka, K., Arakawa, M., 2007. Collisional disruption of weakly sintered porous targets at low-impact velocities. *Earth Planets Space* 59, 319–324.
- Shimaki, Y., Arakawa, M., Yasui, M., 2011. Impact experiments on sintered snowballs. *Proc. Phys. Chem. Ice Conf.* 11, 379–386.
- Suyama, T., Wada, K., Tanaka, H., 2008. Numerical simulation of density evolution of dust aggregates in protoplanetary disks. I. Head-on collisions. *Astrophys. J.* 684, 1310–1322.
- Takagi, Y., Mizutani, H., Kawakami, S., 1984. Impact fragmentation experiments of basalt and pyrophyllites. *Icarus* 59, 462–477.
- Wada, K., Tanaka, H., Suyama, T., Kimura, H., Yamamoto, T., 2009. Collisional growth conditions for dust aggregates. *Astrophys. J.* 702, 1490–1501.
- Yasui, M., Arakawa, M., 2009. Compaction experiments on ice–silica particle mixtures: Implication for residual porosity of small icy bodies. *J. Geophys. Res.* 114, E09004. doi:10.1029/2009JE003374.